J Electroceram (2008) 20:243–249
DOI 10.1007/s10832-007-9188-1

Modeling of a cylindrical ultrasonic motor based on the single crystals

Hua Zhu · Laihui Luo · Chao Chen · Chunsheng Zhao

Received: 27 November 2006 / Accepted: 25 June 2007 / Published online: 2 September 2007

Abstract A novel cylindrical ultrasonic motor based on Pb$(Mg_{1/3}Nb_{2/3})O_3$–$PbTiO_3$ crystals is proposed. Timoshenko beam theory and Lagrange equation are used to analyze the dynamics behavior of the stator. The contact behavior between the hemispherical rotor and the cylindrical stator is simulated by Hertz theory. The general modeling is established to estimate the ultimate performance of the prototype motor. The numerical results and the mechanical measurements from the prototype motor validate the theoretical analysis.

Keywords Ultrasonic motor · Dynamic analysis · Modeling · Simulation

1 Introduction

Ultrasonic motors have superior characteristics, such as high torque at low speed, fast response, simple structure, absence of magnetic interference etc. Because of these advantages, it becomes a good candidate for micro aircraft, medical application and other industrial fields. Piezoelectric ceramics with high energy density are used for the energy conversion from electric to mechanical, so ultrasonic motors have higher output power than other types of motors with the same structural size. One type of ultrasonic motor, the cylindrical ultrasonic motor (CUSM) is more suitable for miniaturization because of its simple structure. Even though many CUSMs with diameters 1–8 mm have been reported, most of them focused on the development of new structural design and new materials [1–4]. A few papers dealt with the driving mechanisms and the dynamic analysis of the stator [5–7]. The investigation of the general model of this type of motor has not been reported yet.

In addition, all of the reported CUSMs used the $Pb(Zr,Ti)O_3$ (PZT) ceramic elements to excite the vibration of the stator. Their applications are limited in low temperatures occasions because of the performance reduction of PZT ceramics. It was discovered that $Pb(Mg_{1/3}Nb_{2/3})O_3$–$PbTiO_3$ (PMN-PT) single crystals have excellent actuation characteristics at cryogenic temperatures [8, 9]. Dong et al. [10] have developed a PMNT linear ultrasonic cryomotor that can operate at 77 K.

So in this study, a new CUSM 4.8 mm in diameter based on PMN-PT single crystals is developed, which is designed for space application. In order to help with the structural design and predict the motor performance as a function of design parameters, an analytical modeling of this motor is first proposed. Timoshenko beam theory and Lagrange equation are used to establish the dynamic modeling of the electromechanical coupling of the stator. Hertz theory is used to treat the frictional contact problem between the hemispherical rotor and the stator. The output performance of the motor is simulated. The numerical results and the mechanical measurements from the prototype motor validate the dynamic analysis.

2 Structure of CUSM based on PMN-PT

Figure 1 illustrates the construction of this motor. The stator consists of four rectangle PMN-PT pieces and a phosphor bronze cylinder. Two hemispherical rotors are designed to reduce the slippage between the rotors and the stator. The

H. Zhu (✉) · C. Chen · C. Zhao
Precision Driving Laboratory, Nanjing University of Aeronautics and Astronautics,
Nanjing, People's Republic of China
e-mail: hzhu103@nuaa.edu.cn

L. Luo
Shanghai Institute of Ceramics, Chinese Academy of Science,
Shanghai, People's Republic of China

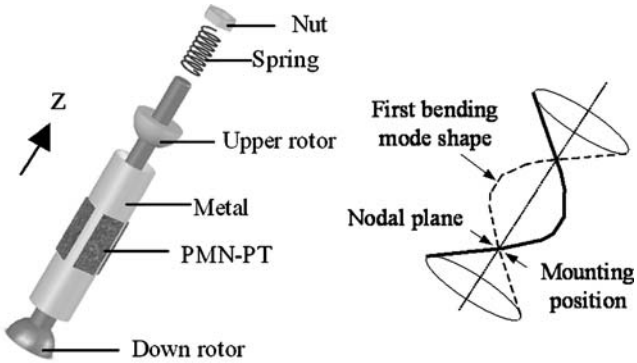

Fig. 1 Structure of cylindrical ultrasonic motor

rotors are pressed against the cylindrical stator by a spring. Its structure is similar as the one developed by Koc et al. [3]. But the configuration of ceramics and driving principle are different. When four pieces of rectangular PMN-PT are excited by voltage signals with specific phase differences as shown in Fig. 2, the wobble motion of the stator will drive the spherical rotors due to the inverse piezoelectric effect. The motor is mounted in the nodal plane of the first bending mode of the stator. Because of the symmetry of the structure, the vibration in x and y direction can be decoupled and analyzed separately.

3 Assumed mode shape of the stator

Considering the ratio of the length and out diameter of the cylinder is 3.5, the rotary inertia of the cross section and shear deformation must be taken into account [11, 12]. Based on the Timoshenko beam theory, without taking account of the single crystals, the assumed mode shape of neutral axis of the metallic cylinder with free–free boundary condition can be defined as

$$W(z) = c_1 \cosh \alpha bz + c_2 \sinh \alpha bz + c_3 \cos \beta bz + c_4 \sin \beta bz \quad (1)$$

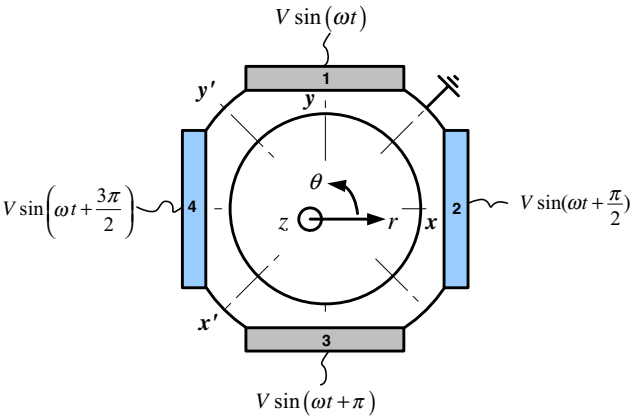

Fig. 2 Configuration of ceramics and the phases of the applied voltages

Fig. 3 Coordinate system of the stator

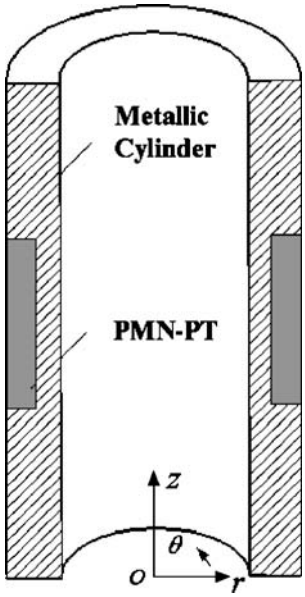

$$\Phi(z) = d_1 \sinh \alpha bz + d_2 \cosh \alpha bz + d_3 \sin \beta bz + d_4 \cos \beta bz \quad (2)$$

where α, β, b can be expressed as

$$\alpha = \sqrt{-\frac{r^2+s^2}{2} + \sqrt{\left(\frac{r^2-s^2}{2}\right)^2 + \frac{1}{b^2}}} \quad (3)$$

$$\beta = \sqrt{\frac{r^2+s^2}{2} + \sqrt{\left(\frac{r^2-s^2}{2}\right)^2 + \frac{1}{b^2}}} \quad (4)$$

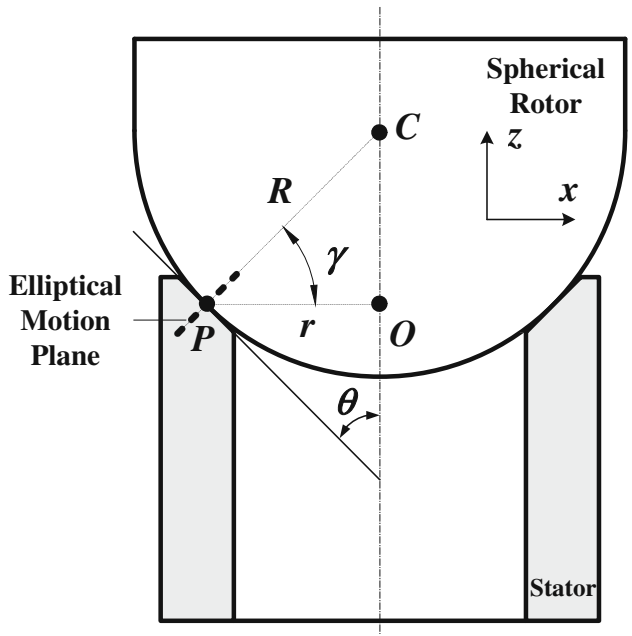

Fig. 4 Taper angle of the stator

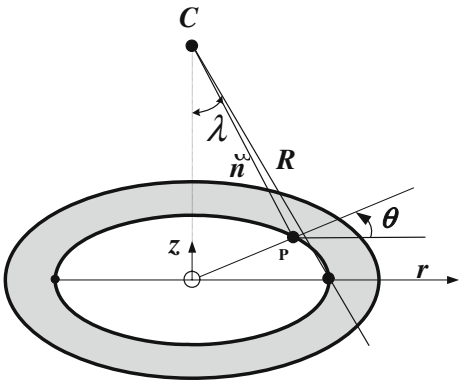

Fig. 5 Displacement in cylindrical coordinate system

$$b^2 = \frac{\rho_m A L^4 \omega^2}{EI} \quad r^2 = \frac{I}{AL^2} \quad s^2 = \frac{EI}{kAGL^2} \tag{5}$$

where L is the length of the stator, I the area moment of inertia of cross section, A the cross-sectional area, ρ_m the density of the metal, G the shear modulus, E the modulus of elasticity, k the numerical shape factor for the cross-section and ω is the natural frequency that can be determined by the following frequency equation

$$2 - 2\cosh b\alpha \cos b\beta + \frac{1}{(1 - b^2 r^2 s^2)^{1/2}} \cdot \left[b^2 r^2 \left(r^2 - s^2\right)^2 + \left(3r^2 - s^2\right) \right] \sinh b\alpha \sin b\beta = 0 \tag{6}$$

Assuming that c_1=1, the coefficients of Eqs. 1 and 2 are related as follows

$$\begin{cases} c_1 = 1 & c_2 = -\lambda\delta & c_3 = \frac{1}{\zeta} & c_4 = -\delta \\ d_1 = \frac{b\left(\alpha^2+s^2\right)}{\alpha L} & d_2 = -\frac{b\lambda\delta\left(\alpha^2+s^2\right)}{\alpha L} & d_3 = \frac{b\left(s^2-\beta^2\right)}{\beta L\zeta} & d_4 = \frac{b\delta\left(s^2-\beta^2\right)}{\beta L} \end{cases} \tag{7}$$

where

$$\lambda = \frac{\alpha}{\beta} \quad \zeta = \frac{\beta^2 - s^2}{\alpha^2 + s^2} \quad \delta = \frac{\cosh b\alpha - \cos b\beta}{\lambda \sinh b\alpha - \zeta \sin b\beta} \tag{8}$$

Table 1 Comparison of the mode frequency via different methods.

Result	I (Eq. 6)	II (Ansys)	III (Eq. 23)	IV (PSV-300 F)
Frequency / Hz	46462	50315	50571	49380
Error	5.9%	1.9%	2.4%	0%

In the cylindrical coordinate system as shown in Fig. 3, when the stator is excited in the first bending mode, the displacement field of the stator can be expressed as

$$\mathbf{u} = \begin{Bmatrix} u_r \\ u_\theta \\ u_z \end{Bmatrix} = \begin{bmatrix} W\cos\theta & W\sin\theta \\ -W\sin\theta & W\cos\theta \\ -r\Phi\cos\theta & -r\Phi\sin\theta \end{bmatrix} \begin{bmatrix} q_1(t) \\ q_2(t) \end{bmatrix} \triangleq \mathbf{N}_m \mathbf{q}(t) \tag{9}$$

where $\mathbf{q}(t)$ is the mechanical modal amplitudes that can be determined through the dynamic analysis of the stator.

4 Dynamic analysis of the stator

According to the geometrical equation, the strain of the stator can be defined as

$$\mathbf{S} = \begin{Bmatrix} \varepsilon_r \\ \varepsilon_\theta \\ \varepsilon_z \\ \gamma_{\theta z} \\ \gamma_{rz} \\ \gamma_{r\theta} \end{Bmatrix} = \begin{bmatrix} \frac{\partial}{\partial r} & 0 & 0 \\ \frac{1}{r} & \frac{\partial}{r\partial\theta} & 0 \\ 0 & 0 & \frac{\partial}{\partial z} \\ 0 & \frac{\partial}{\partial z} & \frac{\partial}{r\partial\theta} \\ \frac{\partial}{\partial z} & 0 & \frac{\partial}{\partial r} \\ \frac{\partial}{r\partial\theta} & \frac{\partial}{\partial r} - \frac{1}{r} & 0 \end{bmatrix} \begin{bmatrix} u_r \\ u_\theta \\ u_z \end{bmatrix} \triangleq \mathbf{B}_m \mathbf{q}(t) \tag{10}$$

To the metallic material, the stress field is expressed as

$$\mathbf{T} = \mathbf{c}_m \mathbf{S} \tag{11}$$

where $\mathbf{c}_m$ is the stiffness matrix of the metallic material.

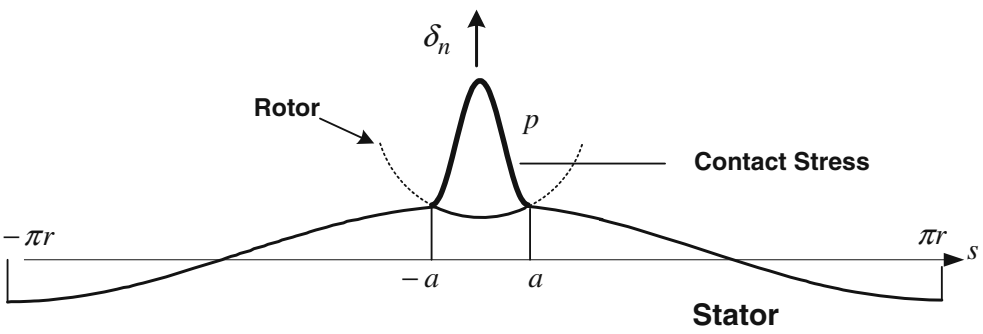

Fig. 6 Contact between the stator and the rotor

Table 2 Material properties of PMN-PT (poled in [110] direction) and the metal.

PMN-PT			Phosphorous bronze			
$[\varepsilon_r^S]$	$[e](\mathrm{C/m^2})$	$\left[C_p^E\right](\times 10^{10}\mathrm{N/m^2})$	Density ρ_p	Young's modulus E	Shear modulus G	Poisson's ratio v	Density ρ_m
$\begin{bmatrix} 857 & 0 & 0 \\ 0 & 640 & 0 \\ 0 & 0 & 405 \end{bmatrix}$	$\begin{bmatrix} 0 & 0 & 0 & 0 & 17.1 & 0 \\ 0 & 0 & 0 & 11.19 & 0 & 0 \\ 14.7 & -9.5 & 5.7 & 0 & 0 & 0 \end{bmatrix}$	$\begin{bmatrix} 18.0 & -31.1 & 8.4 & 0 & 0 & 0 \\ -31.1 & 112.0 & -61.9 & 0 & 0 & 0 \\ 8.4 & -61.9 & 49.6 & 0 & 0 & 0 \\ 0 & 0 & 0 & 14.9 & 0 & 0 \\ 0 & 0 & 0 & 0 & 69.4 & 0 \\ 0 & 0 & 0 & 0 & 0 & 13.0 \end{bmatrix}$	8,090 kg/m^3	113 GPa	41 GPa	0.33	8,800 kg/m^3

To the piezoelectric material, the relation between the strain and the stress can be given as

$$\mathbf{T} = \mathbf{c}_\mathrm{p}\mathbf{S} - \mathbf{e}^T\mathbf{E} \tag{12}$$

where $\mathbf{c}_\mathrm{p}$ is the stiffness matrix of PMN-PT, $\mathbf{e}$ the piezoelectric matrix, $\mathbf{E}$ the electric field in the piezoelectric pieces respectively. If it is assumed that the electric field is equal along the thickness direction of piezoelectric piece, $\mathbf{E}$ can be expressed as

$$\mathbf{E} = \mathbf{B}_e\mathbf{v} \tag{13}$$

where $B_e = 1/h_\mathrm{p}$, h_p is the thickness of PMN-PT pieces, $\mathbf{v}$ is the applied voltage vector.

The Lagrange Equation of this electromechanical coupling vibration system can be written as

$$\left[\frac{\mathrm{d}}{\mathrm{d}\,t}\left(\frac{\partial T_\mathrm{s}}{\partial \dot{q}}\right)\right]^T - \left[\frac{\partial T_\mathrm{s}}{\partial q}\right]^T + \left[\frac{\partial U_\mathrm{m}}{\partial q}\right]^T = \mathbf{F}_\mathrm{s} \tag{14}$$

where $\mathbf{F}_\mathrm{s}$ is the generalized external force.

The kinetic energy $\mathbf{T}_s$ of the stator can be defined as

$$T_\mathrm{s} = \frac{1}{2}\dot{\mathbf{q}}^T\mathbf{M}\dot{\mathbf{q}} \tag{15}$$

with

$$M = \int_{V_\mathrm{m}} \mathbf{N}_\mathrm{m}^T\rho_\mathrm{m}\mathrm{N}_\mathrm{m}\,\mathrm{d}\,V + \int_{V_\mathrm{p}} \mathbf{N}_\mathrm{m}^T\rho_\mathrm{p}\mathrm{N}_\mathrm{m}\,\mathrm{d}\,V \tag{16}$$

where ρ_m is the density of the metal, ρ_p the density of PMN-PT, V_m the volume of the metal, V_p the volume of the PMN-PT.

The potential energy U_m of the metallic cylinder can be defined as

$$U_\mathrm{m} = \frac{1}{2}\mathbf{q}^T\mathbf{K}_\mathrm{m}\mathbf{q} \tag{17}$$

with

$$\mathbf{K}_\mathrm{m} = \int_{V_\mathrm{m}} \mathbf{B}_m^T\mathbf{c}_m\mathbf{B}_m\,\mathrm{d}\,V \tag{18}$$

The external force $\mathbf{F}_\mathrm{s}$ consists of two parts. One is the equivalent excitation force $\mathbf{F}_\mathrm{sp}$ from piezoelectric ceramics, and the other is the mechanical force $\mathbf{F}_\mathrm{sr}$ from the rotor. Based on the virtual power principle, the virtual power P_sp can be defined as

$$P_\mathrm{sp} = \mathbf{F}_\mathrm{sp}^T\dot{\mathbf{q}} = -\int_{V_\mathrm{p}} \mathbf{T}_\mathrm{p}^T\dot{\mathbf{S}}_\mathrm{p}\mathrm{d}V \tag{19}$$

Substituting Eqs. 10 and 11 into 19 results in the following

$$\mathbf{F}_\mathrm{sp} = \Theta\mathbf{v} - \mathbf{K}_\mathrm{p}\mathbf{q} \tag{20}$$

with

$$\Theta = \int_{V_\mathrm{p}} \mathbf{B}_\mathrm{m}^T\mathbf{e}^T\mathbf{B}_\mathrm{e}\,\mathrm{d}\,V \tag{21}$$

$$\mathbf{K}_\mathrm{p} = \int_{V_\mathrm{p}} \mathrm{B}_\mathrm{m}^T\mathbf{c}_\mathrm{p}^E\mathbf{B}_\mathrm{m}\,\mathrm{d}\,V \tag{22}$$

Table 3 Dimensions of PMN-PT pieces and the cylinder.

PMN-PT			The cylinder					
Length	Width	Thinkness	Out-diameter	Inner-diameter	Length	Taper angle	Length of the trough	Depth of the trough
6 mm	2.65 mm	0.5 mm	4.8 mm	3.2 mm	18 mm	45°	6.4 mm	0.4 mm

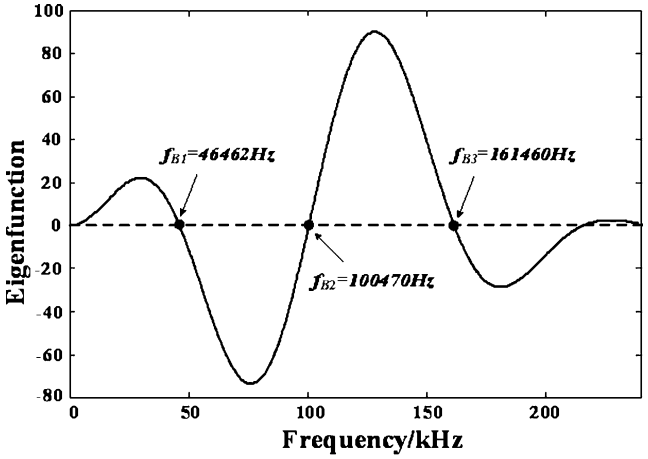

Fig. 7 First three natural frequencies calculated by Timoshenko beam theory

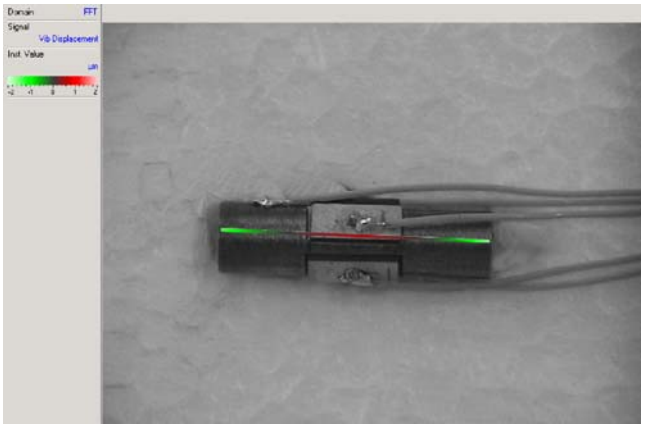

Fig. 9 Mode test of the prototype stator via PSV-300F

Inserting Eqs. 15, 16, 17 and 18 and (20) into (14) leads to the vibration equation of the stator under the excitation

$$\mathbf{M}\ddot{\mathbf{q}} + \mathbf{C}\dot{\mathbf{q}} + \mathbf{K}\mathbf{q} = \Theta\mathbf{v} + \mathbf{F}_{\mathrm{sr}} \tag{23}$$

where $\mathbf{K} = \mathbf{K}_{\mathrm{m}} + \mathbf{K}_{\mathrm{p}}$, $\mathbf{c}$ is the structural damping matrix of the stator. When $\mathbf{F}_{\mathrm{sr}}$=0, Eq. 23 becomes the vibration equation of the free stator.

5 Contact analysis

In order to decrease the radial slippage, a taper angle is designed on the driving surface of the stator as shown in Fig. 4. The radius of the rotor R_{rot} can be given as

$$R_{\mathrm{rot}} = r_{\mathrm{d}}\sqrt{r_{\mathrm{d}}^2\Phi_p^2 + W_p^2}\Big/W_p \tag{24}$$

where r_{d} is the driving radius, W_p and Φ_p are the deflection and bending slope of the driving point P and can be calculated from Eq. 23.

As shown in Fig. 5, the displacement of the driving point P in $\vec{n}$ direction can be expressed as:

$$\delta_n = \Gamma\sin(\omega t + \theta) \tag{25}$$

with

$$\Gamma = W_P\sin\lambda - r_{\mathrm{d}}\Phi_P\cos\lambda \tag{26}$$

and

$$\lambda = \arctan\frac{W_P}{r_{\mathrm{d}}\Phi_P} \tag{27}$$

where ω is the first bending mode frequency of the stator.

Figure 6 illustrates the contact between the stator and the rotor. According to the Hertz contact theory, the contact length a can be given as

$$a = \left(\frac{3R}{4E^*}\frac{F}{\cos\lambda + \mu\sin\lambda}\right)^{1/3} \tag{28}$$

with

$$\frac{1}{E^*} = \frac{1-\mu_{\mathrm{sta}}^2}{E_{\mathrm{sta}}} + \frac{1-\mu_{\mathrm{rot}}^2}{E_{\mathrm{rot}}} \tag{29}$$

$$\frac{1}{R} = \frac{1}{R_{\mathrm{sta}}} + \frac{1}{R_{\mathrm{rot}}} \tag{30}$$

where μ_{sta} is Poisson ratio of the friction material, μ_{rot} Poisson ratio of the rotor, μ the static friction coefficient between the stator and the rotor, E_{sta} Young's modules of the friction material on the stator, E_{rot} Young's modules of the rotor, R_{sta} is the equivalent radius of the stator and $R_{\mathrm{sta}} = r_d^2/\Gamma$.

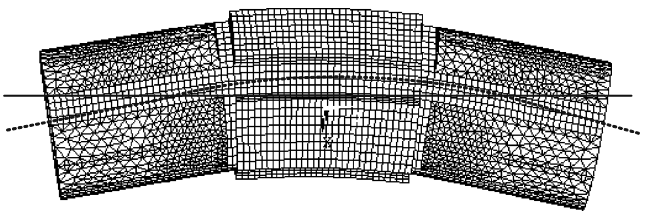

Fig. 8 Modal analysis by ANSYS

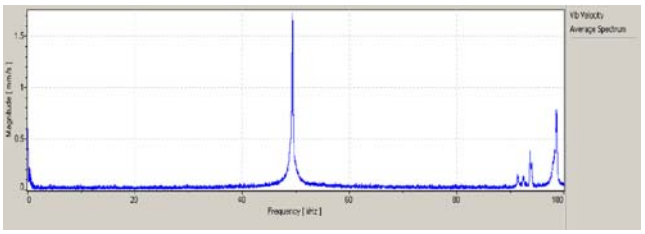

Fig. 10 Modal frequency of the prototype stator

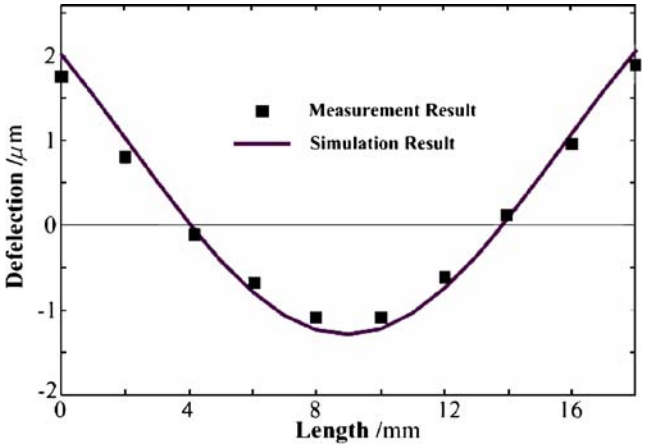

Fig. 11 Deflection of the stator

The distribution of the contact stress p can be expressed as:

$$p = \left(\frac{6E^{*2}}{\pi^3 R^2}\frac{F}{\cos\lambda + \mu\sin\lambda}\right)^{1/3}\sqrt{1-\left(\frac{s}{a}\right)^2} \tag{31}$$

Integrating the driving force in tangential direction over the region of contact can obtain the output torque of the motor:

$$M = \begin{cases} 4\pi\mu_s r_d\left(\int_0^b p(s)s\mathrm{d}s - \int_b^a p(s)s\mathrm{d}s\right) & b \le a \\ 4\pi\mu_s r_d\int_0^a p(s)s\mathrm{d}s & b > a \end{cases} \tag{32}$$

with

$$b = r_d \arccos\frac{v_r}{W_P\omega} \tag{33}$$

where $v_r = r_d\omega_{rot}$, ω_{ro} is the rotational speed of the rotor, μ_s is the friction constant.

6 Simulations and modeling validation

6.1 Modal frequency of the stator with free–free boundary condition

In order to validate our theoretical analysis, we compared the results obtained by different methods as shown in Table 1.

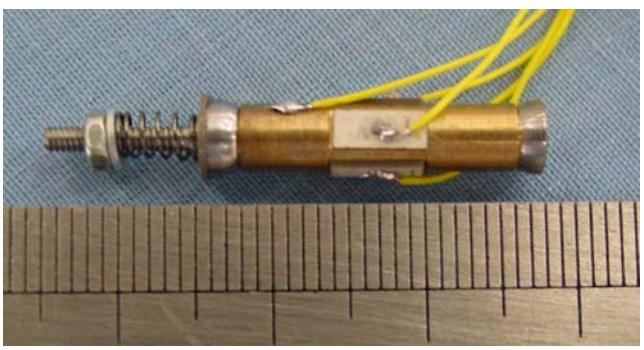

Fig. 12 The prototype CUSM based on PMN-PT

The material parameters and structural parameters used in the simulation are listed in Tables 2 and 3.

The first three mode frequencies are calculated by Timoshenko Frequency Equation (6) as shown in Fig. 7. The first bending frequency of the stator is 46,462 Hz (Result I).

- The mode frequency is also calculated by the finite element method (ANSYS) as shown in Fig. 8 (Result II).
- The mode frequency calculated by the model of this paper (Eq. 23) is 50571 Hz (Result III).
- The prototype motor is manufactured. The dynamic behavior is tested by Polytec Vibration Meter (PSV-300 F) (Result IV). Figures 9 and 10 show the mode shape and the modal frequency of the stator respectively.

The comparison reveals that the model of this paper gives a rather good precision: less than 0.5% of error compared with ANSYS and less than 2.4% of error compared with the mode measurement result of the manufactured stator. The model of this paper is not more accurate than the finite element method but it costs less computing time.

6.2 Displacement response and mechanical performance

Figure 11 shows the displacement response of the stator under the excitation of sinusoidal voltage of 49.4 kHz, 100 $V_{p\text{-}p}$. The square point is the experiment results of the prototype stator via PSV-300 F. The maximum deflection of the stator reaches 1.9 μm. A variation of 5% is obtained between the experimental and simulation results.

Figure 12 is the photo of the prototype motor and its weight is 4.2 g. Figure 13 presents the mechanical performance simulation result of the motor with the experiment points when the driving voltage is 100 $V_{p\text{-}p}$. The pre-pressure between the rotor and the stator is 2.1 N. From this figure, we can find that the model in this paper

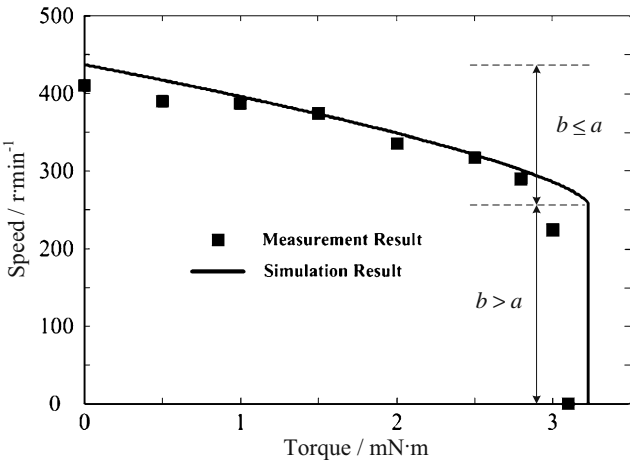

Fig. 13 Simulation of the mechanical performance

can predict the maximum output torque of the motor accurately. Figure 13 also reveals that when the torque applied to the motor is increased from 0 to 2.8 mN m, the output speed will decrease gradually from about 400 to 250 rpm, whereas the torque increased further to the stall value 3.2 mN m, the motor speed drops. This phenomenon is due to the small contact area caused by the small pre-pressure. When the motor speed is low (below 250 rpm, $b>a$), the driving points in the contact area is moving faster than the rotor, so the whole area is driving the rotor, the output torque of the motor is stable while the motor speed increases. But when the motor speed is higher (above 250 rpm, $b\leq a$), the contact area is divided into two parts. In one part of area, the driving points are moving faster than the rotor, so this part is driving the rotor. In another part of area, the driving points are moving slower and this part is obstructing the rotor. Further more, with the increasing of the motor speed, the obstructing area becomes larger. So the output torque of the motor decreases as the motor speed is on a rise.

7 Conclusion

A new CUSM is present based on the piezoelectric material PMN-PT. Lagrange equation provides a feasible approach to solve the dynamic problem of electromechanical systems. The global modeling is established and it can be used as a design tool to predict the performance of the future motor or optimize the structural parameters. Further study on the nonlinearity behavior of the friction will be helpful to improve the accuracy of the simulation.

References

1. T. Morita, M.K. Kurosawa, T. Higuchi, A cylindrical micro ultrasonic motor using PZT thin film deposited by single process hydrothermal method (φ2.4 mm, L=10 mm stator transducer), IEEE Trans. Ultrason. Ferroelectr. Freq. Control, **45**(5), 1178–1187 (1998)
2. T. Morita, M.K. Kurosawa, T. Higuchi, A cylindrical shaped micro ultrasonic motor utilizing PZT thin film (diameter 1.4 mm and L5.0 mm stator transducer), Proc. of Int. Conf. on Solid-state, Sensor and Actuators, Transducers 99, Sendai, **2**, 1744–1747 (1999)
3. B. Koc, S. Cagatay, K. Uchino, A piezoelectric motor using two orthogonal bending modes of a hollow cylinder, IEEE Trans. Ultrason. Ferroelectr. Freq. Control, **49**(4), 495–500 (2002)
4. S. Dong, S.P. Lim, K.H. Lee, J. Zhang, et al., Piezoelectric ultrasonic micromotor with 1.5 mm diameter, IEEE Trans. Ultrason. Ferroelectr. Freq. Control, 361–367 (2003)
5. P. Lu, K.H. Lee, S.P. Lim, W.Z. Lin, A kinematic analysis of cylindrical ultrasonic motors, Sens. Actuators, **A87**, 194–197 (2001)
6. T. Morita, M. Kurosawa, T. Higuchi, An ultrasonic micromotor using a bending cylindrical transducer based on PZT thin films, Sens. Actuators, **A50**, 75–80 (1995)
7. X. Wang, C.J. Ong, C.L. Teo, S.K. Panda, "Dynamic analysis of cylindrical ultrasonic motor under external excitation, Sens. Actuators, **A105**, 247–254 (2003).
8. S.E. Park, V. Vedula, M.J. Pan, et al., Relaxor based ferroelectric single crystals for electromechanical actuators, Proc. SPIE Int. Soc. Opt. Eng., **3324**, 136–144 (1998)
9. D.S. Paik, S.E. Park, T.R. Shrout, et al., Dielectric and piezoelectric properties of perovskite materials at cryogenic temperature, J. Mater. Sci. **34**(3), 469–473 (1999)
10. S. Dong, L. Yan, N. Wang, et al., A small, linear, piezoelectric ultrasonic cryomotor, Appl. Phys. Lett. **86**, 053501 (2005)
11. S.P. Timoshenko, *Vibration problems in engineering, third edition* (D.Van Nostrand, New York, 1995)
12. T.C. Huang, The effect of rotatory inertia and of shear deformation on the frequency and normal mode equations of uniform beams with simple end conditions, J. Appl. Mech. 579–584 (1961)